PHYSICAL REVIEW E **83**, 021306 (2011)

Bubbling in vibrated granular films

Piroz Zamankhan[*]

Faculty of Industrial, Mechanical Engineering, and Computer Sciences, University of Iceland, Hjardarhagi 2-6, IS-107 Reykjavik, Iceland

(Received 25 September 2010; revised manuscript received 4 January 2011; published 28 February 2011)

With the help of experiments, computer simulations, and a theoretical investigation, a general model is developed of the flow dynamics of dense granular media immersed in air in an intermediate regime where both collisional and frictional interactions may affect the flow behavior. The model is tested using the example of a system in which bubbles and solid structures are produced in granular films shaken vertically. Both experiments and large-scale, three-dimensional simulations of this system are performed. The experimental results are compared with the results of the simulation to verify the validity of the model. The data indicate evidence of formation of bubbles when peak acceleration relative to gravity exceeds a critical value Γ_b . The air-grain interfaces of bubblelike structures are found to exhibit fractal structure with dimension $D = 1.7 \pm 0.05$.

DOI: 10.1103/PhysRevE.83.021306 PACS number(s): 45.70.−n

I. INTRODUCTION

Vibrating layers of fine brass balls form themselves into fascinating patterns called oscillons at critical amplitude [1]. This self-sustaining state was named by analogy with the soliton. The soliton is a localized wave packet or pulse that maintains its integrity while traveling at a constant speed. Oscillons have been observed experimentally to arise from collisions between brass balls in an evacuated, vertically vibrated, granular layer.

When layers of sand immersed in air in a thin annular geometry are vibrated vertically by $z = A\sin(\omega t) \leqslant$, bubbling behavior has been observed [2]. Note that for adequate air-grain coupling, the Stokes number, defined as $\mathrm{St} = \tau U_0/\sigma$, should not exceed 5000 [3]. In this light, the requirement of adequate air-grain coupling sets an upper grain size limit to $\sigma = 400\ \mu\mathrm{m}$ [3]. Here, τ is the relaxation time of the grain, defined as $\beta\sigma^2/18\nu$, σ is the particle diameter, β is the grain-to-air density ratio, ν is the air kinematic viscosity, and U_0 is the velocity of the air flow well away from the grain.

If the peak acceleration relative to gravity, $\Gamma = A\omega^2/g$, exceeds unity, then the layers of sand will be projected upward, return, and will settle within the same vibration cycle. This process will be repeated in each successive cycle. Hence $\Gamma > 1$ is a necessary condition for sustained flow [2]. When the sand is projected upward, air will be drawn downward, and later as the sand settles the air will be pushed upward through it. It is known that cyclical movements of air through sand can induce convection in such a system [4].

Pak and Behringer [2] made Γ sufficiently high that the sand had not fully settled when it was thrown up again. The compressed air trapped in the sand expanded when the sand was projected and formed bubbles.

Fingerlike structures have been observed from inside bubbles [2]. The physics behind this phenomenon is still being debated. In Newtonian fluids, the competing effects of viscosity and surface tension result in a frontal fingering instability. It is unclear whether analogous effects explain the fingering patterns observed in dense granular flows. Note that it has become common to regard a flowing granular assembly as a fluid with zero surface tension [5].

The dynamics of dense granular flows such as those reported above remain poorly understood, although they have large industrial applications in, for example, pharmaceuticals, food handling, and the mixing of building materials. Specifically, a better understanding of the mechanism of bubbling would bring substantial benefits by enabling optimizations of processes and transport for a number of industries, including the oil industry.

The objective of the current work is to develop a generalized fluid-particle model with the help of experiments, computer simulations, and a theoretical investigation. The model will be used to investigate the flow dynamics of dense granular media immersed in air in an intermediate regime where both collisional and frictional interactions may affect the flow behavior. The fluid dynamics is solved using a simplified multiscale method [6] while the grain dynamics is computed through molecular-type dynamics [7].

The model is validated by its accuracy in describing bubbling behavior in vertically shaken granular films in a shaker, as detailed in the following section. The validated model is used to investigate a number of observed phenomena in vertically vibrated air-grain systems including the Faraday tilting response to vertical vibration, bubbling, turbulent granular films, and granular fingering instability.

The organization of the paper is as follows. In Sec. II, the experimental apparatus is described and some experimental results are presented. In Sec. III, the mathematical model is presented for solid particles immersed in air. In Sec. IV, the developed model is applied to the specific example of vertically shaken granular films. The simulation results for bubbling and turbulent granular films are presented. Qualitative as well as quantitative comparisons with the experimental results are made to verify the validity of the model. The phenomena caused by cyclic motion of air through the granular assembly are discussed in the same section. Concluding remarks are presented in Sec. V. The present attempt may contribute to a more homogeneous theory of gas-fluidized beds, which has received little attention in the research literature but has grown in importance in recent years.

---

[*] piroz@hi.is

II. EXPERIMENTAL APPARATUS: PROCEDURE AND RESULTS

A frontal view of the apparatus is illustrated in Fig. 1(a). The apparatus consists of a mechanical shaker (PASCO SF-9324) with a straight driving shaft, a signal generator, a power amplifier, a connector box, and a cell. The signal generator generates sine voltage waves with controllable amplitude and frequency as the input to the power amplifier. The current is then amplified and sent to the mechanical shaker through the connector box. The cell, which is connected to the driving shaft, consists of two concentric thin-walled Plexiglas cylinders. The radius of the inner cylinder is $R_0 = 3$ cm. The radial gap between the cylinders is $t = 2.1$ mm. The vibration axis is the cylindrical axis.

Figure 1(b) presents a sketch of the cell. The granular material consists of spherical glass beads with diameter $\sigma = 330 \pm 55\ \mu$m. The physical properties of the glass beads are listed in Table I.

A frontal view of the cell is given in Fig. 1(c). As can be seen from Fig. 1(c), the inner cylinder is painted to enable the taking of dark background images. This facilitates the morphological opening operation to estimate the background illumination in the image processing and analysis [8]. The granular response to vertical vibration is registered using high-speed photography. In this study, the grains are relatively large so that the observation of the motion of individual grains is possible. However, experiment alone does not suffice to identify the physical mechanism behind bubbling. It is complemented by computer simulations that assist in the interpretation of the results.

The heights of the inner and outer cylinders are $H_{vin} = 12$ cm and $H_{vout} = 8.5$ cm, respectively. The glass beads as illustrated in Fig. 1(c) partially fill the cell up to the level of free surface at $H_0 = 4.2$ cm. Figure 1(d) shows the top view of the cell.

TABLE I. Physical properties of glass beads.

Physical Properties	
Density	2.5 kg/m^3
Young's modulus	63 GPa
Hardness	⩾6 Mohs
Specific thermal conductivity	1.129 W/K m
Coefficient of expansion	9.05 106 1/K (20 − 400 °C)
Specific thermal capacity	1.329 kJ/kg K (>600 °C)
Softening point	734 °C
Melting point	1446 °C
Single-particle terminal velocity	2.277
Analysis	
SiO_2	72.50%
Na_2O	13.00%
CaO	9.06%
MgO	4.22%
Al_2O_3	0.58%

The total number of glass beads in the system may be estimated as 4.5×10^5, which is 20 times less than the number of particles used in the experiments in [2]. Recently, Zamankhan [9] has demonstrated that large-scale, three-dimensional computer simulations of air-grain mixtures can be performed on a single graphics processing unit (GPU). He has suggested that large-scale simulations of a system as illustrated in Fig. 1(c) at interactive rates would be feasible using several GPU's.

Some electrostatic attraction between the beads and the cell walls builds up during shaking. At higher values of Γ, an antistatic agent should be added to aid photography. The additives may not affect the granular separation. Note that the beads should be baked before use to minimize the bed moisture content, which causes cohesion between grains [5].

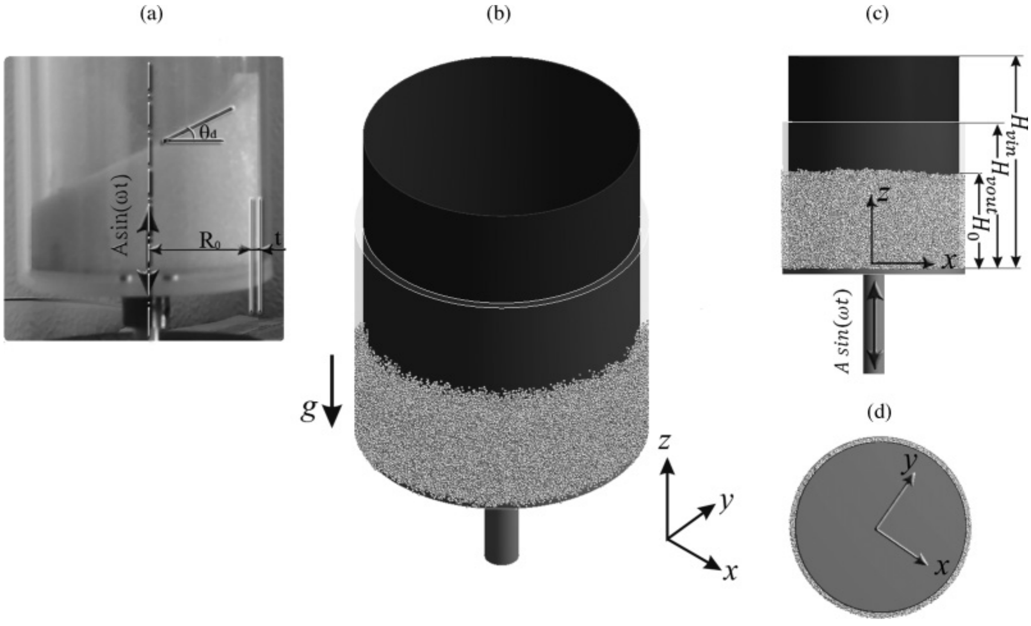

FIG. 1. (a) An image of the apparatus. The radius of the inner cylinder is $R_0 = 3$ cm. The radial gap between the cylinders is $t = 2.1$ mm. (b) Sketch of the apparatus used in simulations. (c) A side view of the cell with some nomenclatures. (d) A top view of the cell.

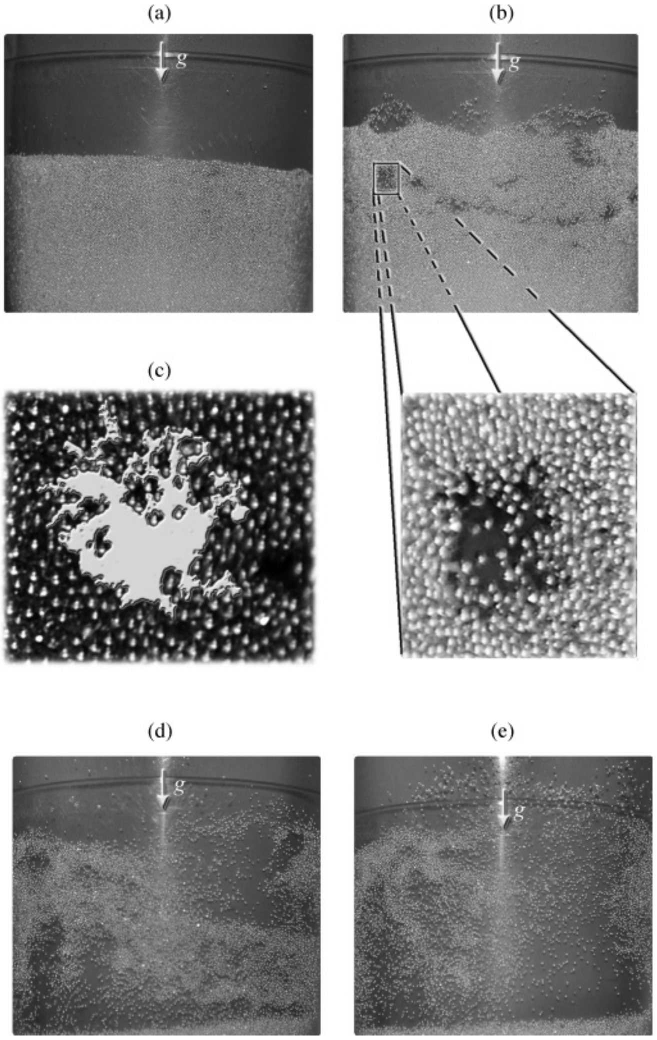

FIG. 2. (a) Images of bubbling and turbulent granular films. Small voids are observed at the free surface at $\Gamma = \Gamma_b = 5$. (b) Bubbling in vertically vibrated granular film at $\Gamma = 6.5$, $\omega/2\pi = 31$, $A = 0.17$ cm, and $H_0 = 4.2$ cm. Inset: singularity along the air-grain interface. (c) Finger patterns in a bubblelike structure in (b). The light regions in the image are void areas where the air displaced the grains. (d) and (e) Turbulent granular films at $\Gamma = 10$ and 11, respectively.

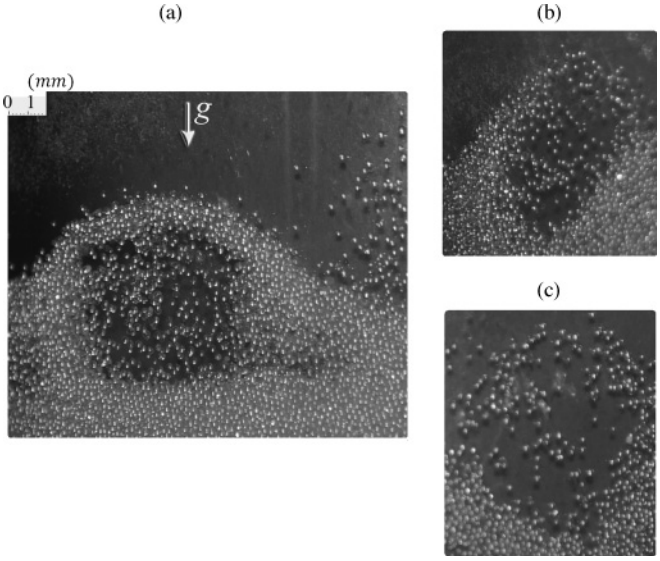

FIG. 3. (a) An image of a large bubblelike structure at the free interface. (b) Bubble bursting through the interface into air. (c) Bubble collapsing leaving a depression and two heaps. Here, $\Gamma = 7.05$, $\omega/2\pi = 32$, $A = 0.17$ cm, and $H_0 = 4.2$ cm.

The granular material is vibrated so that the free surface becomes unstable at $\Gamma \approx 1.2$. The peak acceleration is varied by changing ω at fixed A. As can be seen in Fig. 1(a), the vertically vibrated grain assembly tilts and the tilt angle reaches a dynamic angle of repose, θ_d, at $\Gamma \approx 2$. The cohesive force between the beads may be estimated from the angle of repose [5].

The Faraday tilting effect weakens when Γ exceeds 2. At $\Gamma \geqslant \Gamma_b = 5$, small voids having the quality of bubbles in fluidized bed [10] are observed at the free surface, as illustrated in Fig. 2(a). The mean size of bubbles increases as Γ increases. Figure 2(b) illustrates large bubbles approaching the free surface and bursting through it. Here, $\Gamma = 6.5$, $\omega/2\pi = 31$, $A = 0.17$ cm, and $H_0 = 4.2$ cm. As can be seen from Fig. 2(b), singularities can be found along the bubblelike interfaces. The singularities are magnified and replotted in the inset. Figure 2(c) clearly shows fingerlike patterns in a bubble in the vibrated granular film experiments. Note that the singularities and fractal structures shown in Fig. 2(c) are not similar to those structures found in Ref. [5]. Viscous fingering only happens in a Hele-Shaw geometry. However, fingering patterns in the bubbles and viscous fingering may be remotely related.

Figures 2(d) and 2(e) represent turbulent granular films. In these cases, Γ equals 10 and 11, respectively. It is quite difficult to control the shaker and carry out useful experiments at very high values of Γ.

Figure 3(a) illustrates a clear snapshot of a large bubblelike structure at the free interface. The experimental parameter values are $\Gamma = 7.05$, $\omega/2\pi = 32$, $A = 0.17$ cm, and $H_0 = 4.2$ cm. The beads in Fig. 3(a) are nearly monodisperse. Unlike the granular gas case, diffusion of grains in a dense granular flow is very limited, and therefore the two grains may remain neighbors for a long time. In this situation, grain-grain interactions mainly occur through inelastic, frictional collisions that may not conserve kinetic energy but do conserve momentum. In a dense granular flow, a tagged grain collides initially with a neighbor, and then slightly diffuses through the gas, suffering collisions with other neighboring grains, before colliding with the same grain it collided with initially. These collision events at the low relative velocities of the grains could lead to the formation of cohesive bridges whose strength increases with the contact time and decreases with the increase of the (slipping) relative velocity. In this light, it may be conjectured that inelastic, frictional collisions between grains give rise to a collective behavior such as the formation of granular bridges that are nonstraight and chainlike structures. They cause compressed air to be trapped and change the behavior of the system significantly. The aforementioned bridges may induce jamming and the mixture will become effectively rigid [11]. For the sake of brevity, the adhesive granular bridges will be called chains henceforth.

Figure 3(b) illustrates a bubble bursting through the interface into air. As can be seen from Fig. 3(b), the stress distribution due to frictional contact between the grains in the assembly could not balance the air pressure, which violates the yield condition. Hence, dense granular flows possess properties of a viscoplastic fluid [12]. Figure 3(c) shows a bubble collapsing leaving a depression and two heaps. Air-immersed granular beds under vibration are examples of nonlinear systems. In the following section, a theoretical framework will be presented to aid their understanding.

III. MODEL DESCRIPTION

The effects described in Fig. 3(a) involve interactions between air and beads. The physical mechanisms behind these can only be identified with the help of simulations. The systems illustrated in Fig. 3 contain a large number of chainlike structures, which are aggregates of beads. Aggregation phenomena in dense granular flows are still poorly understood.

Consider a simple granular chain, as illustrated in Fig. 4(a), with both ends supported, consisting of 11 beads, each with a diameter $\sigma = 330\ \mu\text{m}$. The beads are tightly packed together and they overlap slightly. Their coefficient of static friction is $\mu_s = 0.6$ [7]. Rabinowicz [13] suggested that the coefficient of kinetic friction depends on the relative velocity of slipping. It decreases with an increase in velocity. The coefficient of kinetic friction of beads may be estimated as $\mu_d = \tan(\theta_d)$, where θ_d is the dynamic angle of repose. Thus from Fig. 1(a) the value of the coefficient of dynamic friction for beads may be estimated as $\mu_d = 0.47$. In this study, the rate- and state-dependent model of Rice and Ruina [14] is utilized to take into account the dependence of the coefficient of kinetic friction on the relative velocity of slipping. According to the aforementioned model [14], the coefficient of kinetic friction may be represented by the following expression:

$$\mu_c = \mu_d + (\mu_s - \mu_d)\, e^{-C V_{\text{rel}}}, \tag{1}$$

where C is the exponential decay coefficient and V_{rel} is the relative velocity of the surfaces in contact. The exponential decay coefficient is the quantity not known in advance; it may be extracted from the data.

The initial stress distribution in the chain is calculated using Galerkin methods as described in [15]. Figure 4(b) illustrates the contours of the effective (von Mises) stresses [16], σ_{eff}, caused by initial overlapping. The contours for stress are plotted on an xy plane cutting through the axis of symmetry of the granular chain. Figures 4(c) and 4(d) show the contours of the shear, τ_{xy}, and normal stresses, σ_{xx}, respectively, on the same cutting plane.

Consider the case in which the lower side of the *floating chain* is exposed to air pressure above ambient $\Delta p = 20$ Pa while the upper side is exposed to ambient pressure. The effect of gravity is neglected. The following question arises: Does the air pressure difference violate the yield condition?

To address this issue, the variational multiscale method (VMS) is used as described by Jafari, Zamankhan, Mousavi, and Hentinen [6]. In the simulation, $\delta t = 5 \times 10^{-8}$ s is used as the time step. Figure 4(e) illustrates the displacement of grains as a function of time. The last two configurations in Fig. 4(e) illustrate breach formation and eventual chain failure, respectively. The breach is the small opening formed in the chain when it yields. When the chain is breached, air flows through the gap into the downstream area. As can be seen from the last two configurations in Fig. 4(e), once a developing breach has been initiated, the discharging air erodes the chain until complete failure. Here, it is assumed that the chain failed completely and instantaneously because the last two configurations are separated by only $t = 10^{-4}$ s, which is too short compared to that required for the chain to yield. In this case, the chain yields after $t_{\text{chain}} = 4 \times 10^{-3}$ s. Here, t_{chain} represents *the chain lifetime* of a simple chain, named after its closest time-scale analogy, the eddy lifetime [17].

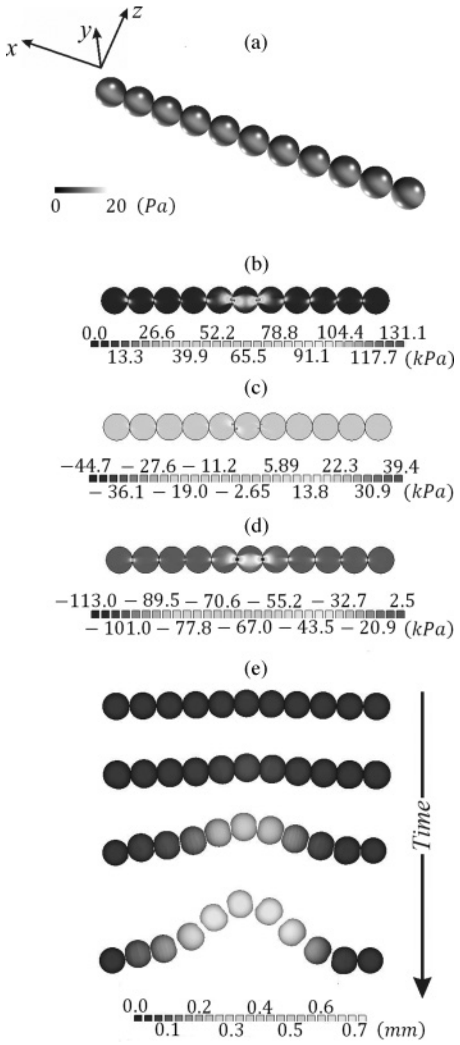

FIG. 4. (a) Sketch of a floating granular chain exposed to air pressure. The grain size is $\sigma = 330\ \mu\text{m}$. (b) Contours of the effective (von Mises) stresses, σ_{eff}, caused by initial overlapping on an xy-plane cutting through the axis of symmetry of the granular chain. (c) and (d) Contours of the shear, τ_{xy}, and normal stresses, σ_{xx}, respectively, on the same cutting plane as in (b). (e) The computed displacement of grains as a function of time. The chain becomes finally unstable at $t = 4 \times 10^{-3}$ s.

In light of the above analysis, it is expected that chainlike structures in air immersed beds under vibration undergo rapid deformations with existing chainlike structures collapsing and

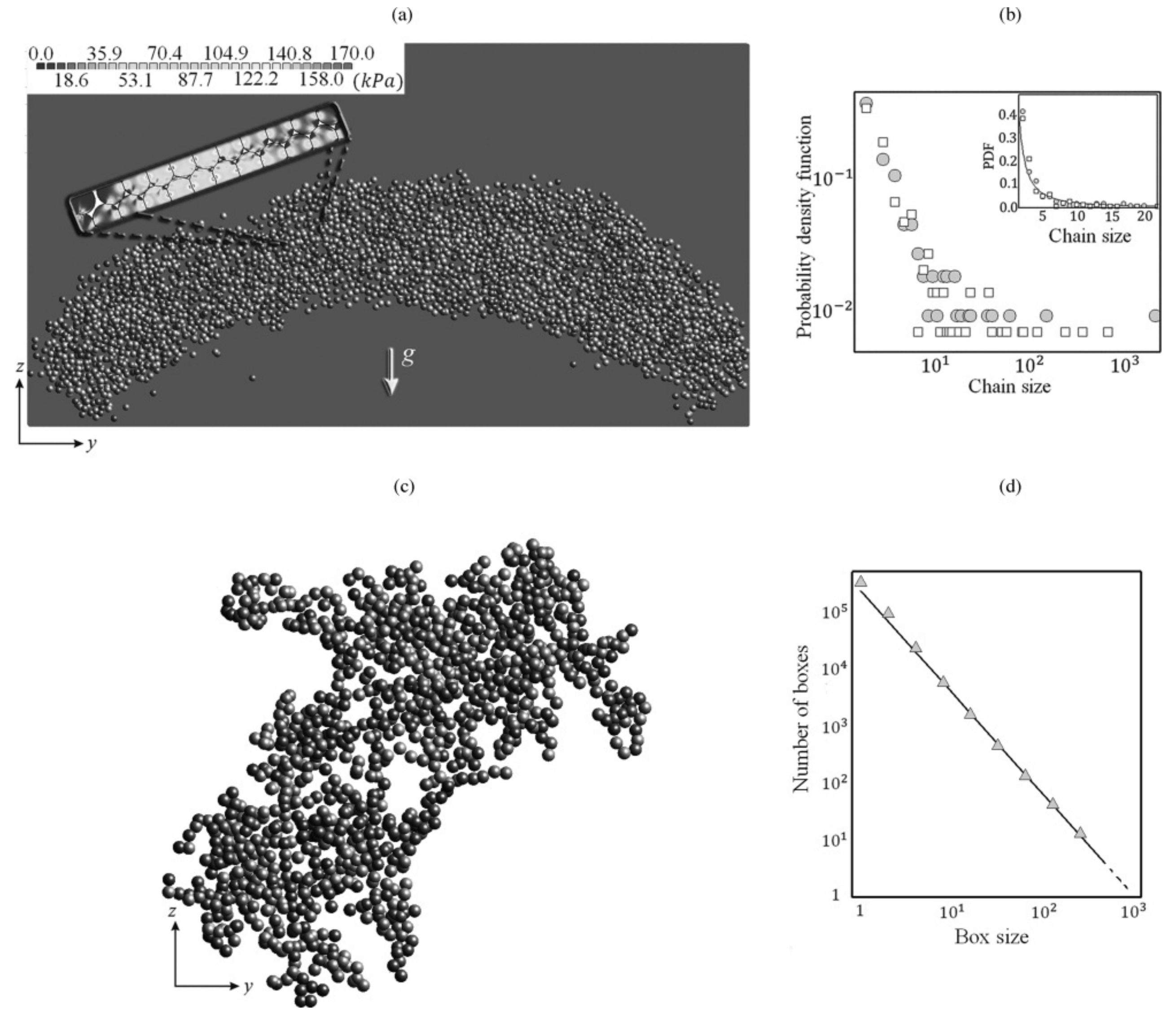

FIG. 5. (a) A chainlike structure hundreds of particles long. Inset: Contours of the instantaneous effective stresses, σ_{eff}, on a cutting yz plane for a chain sample taken from the central part of the particulate assembly. Air is forced into the ensemble from the lower part. Here, Δp between the lower and upper parts is 60 Pa. (b) The chain size distribution. Circles represent the distribution before air-grain interactions and squares show the distribution after 0.01 s. Inset: The chain size distribution for lengths up to 20 beads. (c) A typical large chain in the ensemble. (d) Number of boxes of size R needed to cover the chain. Here, the fractal scales as $R^{1.72}$.

new ones being generated. The objective is to investigate the evolution of the chain size distribution in a given particulate assembly, as shown in Fig. 5(a). The assembly, which closely resembles the upper part of a bubble, consists of a large number of chainlike structures at time t. It is a 1:1.2 scale of a structure that has been found in earlier computer simulations of a vertically vibrated bed of grains reported in Ref. [9]. Compressed air with pressure above ambient $\Delta p = 65$ Pa is blown through it. The circles in Fig. 5(b) show the probability of a bead belonging to a chainlike structure of size i at time t.

A mesh-free [18] version of VMS is used to examine the evolution of the resulting chainlike structures due to the driving pressure difference, Δp. The coefficient of friction is calculated using Eq. (1) and the physical properties of glass beads are listed in Table I. The inset of Fig. 5(a) illustrates the contours of the instantaneous effective stresses, σ_{eff}, for a chain sample taken from the central part of the particulate assembly. The contours are plotted on a cutting yz plane at time t.

The spheres and squares in Fig. 5(b) represent the computed chain size distribution of two configurations at the initial stage, $t = 0$, and the late stage, $t = 0.01$ s, respectively. As can be seen from Fig. 5(b), there exists a very large chainlike structure at the initial stage whose size is more than 5000 grains. This chain breaks down at the late stage and smaller ones are formed that resist air pressure more effectively. The inset shows the chain size distribution for lengths up to 20 grains. Note that the size distribution of shorter chainlike structures does not change with time and remains very similar to a *Schulz* distribution.

Figure 5(c) shows a typical computed large chain in the assembly. As can be seen from Fig. 5(c), it is a fractal. It is known that the grain-gas interfaces exhibit fractal structures, which may be associated with fluid fingering in the zero-surface-tension limit [5]. As stated earlier, fractal structures found in Ref. [5] are not similar to the structure shown in Fig. 5(c).

To quantify the fractal dimension of the chain, the box-counting method is used. Figure 5(d) illustrates the number of boxes of size R needed to cover the chain. The lower bound corresponds to 0.88σ. In Fig. 5(d), a solid line is fitted whose slope is 1.72. Thus the fractal in Fig. 5(c) appears to scale as $R^{1.72}$. It is worth mentioning that a fractal object requires infinitely many orders of magnitude of power-law scaling [19]. In this light, the structure depicted in Fig. 5(c) is called fractal-like. In Sec. IV C, fractal-like structures will be presented whose fractality holds over nearly three orders of magnitude.

The Kolmogorov dimension of the chain in Fig. 5(c) closely resembles that of a diffusion-limit-aggregation (DLA) pattern, $D = 1.7 \pm 0.02$ [20]. A common approach for obtaining the 3D fractal dimension of a chain is adding one to its corresponding 2D fractal dimension assuming uniform mass distribution of the chain along the third dimension. However, this approach is debated [21].

A. Shear viscosity of chainlike structures

The stress tensor in a granular fluid has the following form [22]:

$$\sigma_{\alpha\beta} = -\frac{1}{V_k}\left(\sum_{i=1}^{N_k} m_i C_{i\alpha} C_{i\beta} + \sum_{i=1}^{N_k}\sum_{j>1}^{N_k} r_{ij\alpha} f_{ij\beta}\right), \tag{2}$$

where $C_{i\alpha} = V_{i\alpha} - u_\alpha$ is the α component of the fluctuation velocity of bead i, $u_\alpha = 1/N_k \sum_{i=1}^{N_k} V_{i\alpha}$ is the α component of mean velocity, N_k is the number of beads in the sampling volume V_k, $r_{ij\alpha} = r_{j\alpha} - r_{i\alpha}$ is the α component of the vector connecting the center of bead j to bead i, and $f_{ij\beta}$ is the β component of force on bead i due to bead j $(\alpha,\beta = x,y,z)$.

Consider next the expression for shear viscosity [22],

$$\eta = \frac{V_k}{\sigma T^{1/2}} \int_0^\infty dt \langle \sigma_{\alpha\beta}(t)\sigma_{\alpha\beta}(0)\rangle, \tag{3}$$

where $\sigma = 1/3 \sum_\alpha \sigma_{\alpha\alpha}$ and $\delta\sigma(t) = \sigma(t) - \langle\sigma\rangle$, and the brackets represent an average value. Goldrisch and von Noije [23] have argued that the single-particle distribution functions (in vibrated moderately dense granular fluids) are strongly non-Gaussian. In this case, semiphenomenological approaches based on the application of the Enskog-Boltzmann equation may fail to account for correlated collisions, which are of importance in moderately dense and dense granular fluids. They have suggested that the averages in Eq. (3) should be computed over the homogeneous ensemble. They also proposed a nonperturbative method for computing η.

As stated earlier, inelastic, correlated collisions between grains may result in a collective behavior such as the formation of chainlike structures. For the polydisperse chain mixture shown in Fig. 5(a), the shear viscosity may be given as

$$\eta \sim T^{1/2} \int_0^\infty f(R) S(R)\, dR, \tag{4}$$

where $f(R)$ represents the Schulz distribution of chain size R, given by

$$f(R) = \frac{e^{-(z+1)R/\overline{R}}}{z!} [(z+1)R/\overline{R}]^z. \tag{5}$$

Here, $\overline{R}$ is the mean chain size and $S(R)$ is to be determined from the polydisperse kinetic type theory as described in [24]. As shown in the preceding section, the mass per chain is proportional to the linear size of the chain raised to the Dth power. The mass-size distribution is given as

$$m(R) = \frac{\overline{m}\, R^D}{\int_0^\infty f(R) R^D dR}, \tag{6}$$

where $\overline{m} = \int_0^\infty f(R) m(R) dR$ is the average mass per chain. It can be shown that the shear viscosity increases as the variance (or polydispersity) increases. In addition, the shear viscosity diverges as the solid volume fraction increases. Rosensweig [25] has suggested that if the particles of a particulate assembly have a tendency to form chains, the value of solid volume fraction at which it becomes an effectively rigid system is much less than that corresponding to close packing of spheres. The full theory and the dependence of the shear viscosity of the particulate assembly on the granular temperature, the coefficient of restitution, the mean chain size $\overline{R}$, and the average mass per chain $\overline{m}$ are beyond the scope of this work and will be taken up elsewhere.

The mesh-free version of VMS is a promising approach for simulating air-immersed granular beds. However, real-world applications over long simulation runs of 10^8 time steps and more will probably remain intractable in the foreseeable future. Therefore, a simplified version of VMS will be introduced here in which the air-grain coupling is treated through an empirical mean-field approach and grain-grain collisions are modeled using a phenomenological model based on the modified Kelvin-Maxwell model [7].

B. Models for the gaseous phase

The VMS [6], formulated as a variational approach, is promising. In this approach, the air-grain coupling is treated based on individual grains. Figure 6(a) shows a computed instantaneous air flow field in an air-immersed granular bed under vibration on a cutting xz plane. Here, a bubble bursts through the interface into air creating a spray of beads. For this case, $\Gamma = 7.05$, $\omega/2\pi = 32$, $A = 0.17$ cm, and $H_0 = 4.2$ cm. The richness of the air flow structures is evident from the inset of Fig. 6(a). It is worth mentioning that beads in free flight will feel the eddylike, erratic structures of the instantaneous air flow field, not the smooth average field. This should be taken into account when developing a simplified version of VMS.

Figure 6(b) illustrates the instantaneous coarse-mesh resolved air flow field for the aforementioned case. In this system, beads are not subject to a uniform flow. Instead, a force called Saffman lift [26] comes into play because of the velocity difference between the flows past a grain on different sides. The grain tends to move toward the side with lower pressure. A transverse migration of the grain can occur under the effect of the Saffman lift causing the beads in a chain to slip relative to each other, which makes the chain weaker and its lifetime shorter.

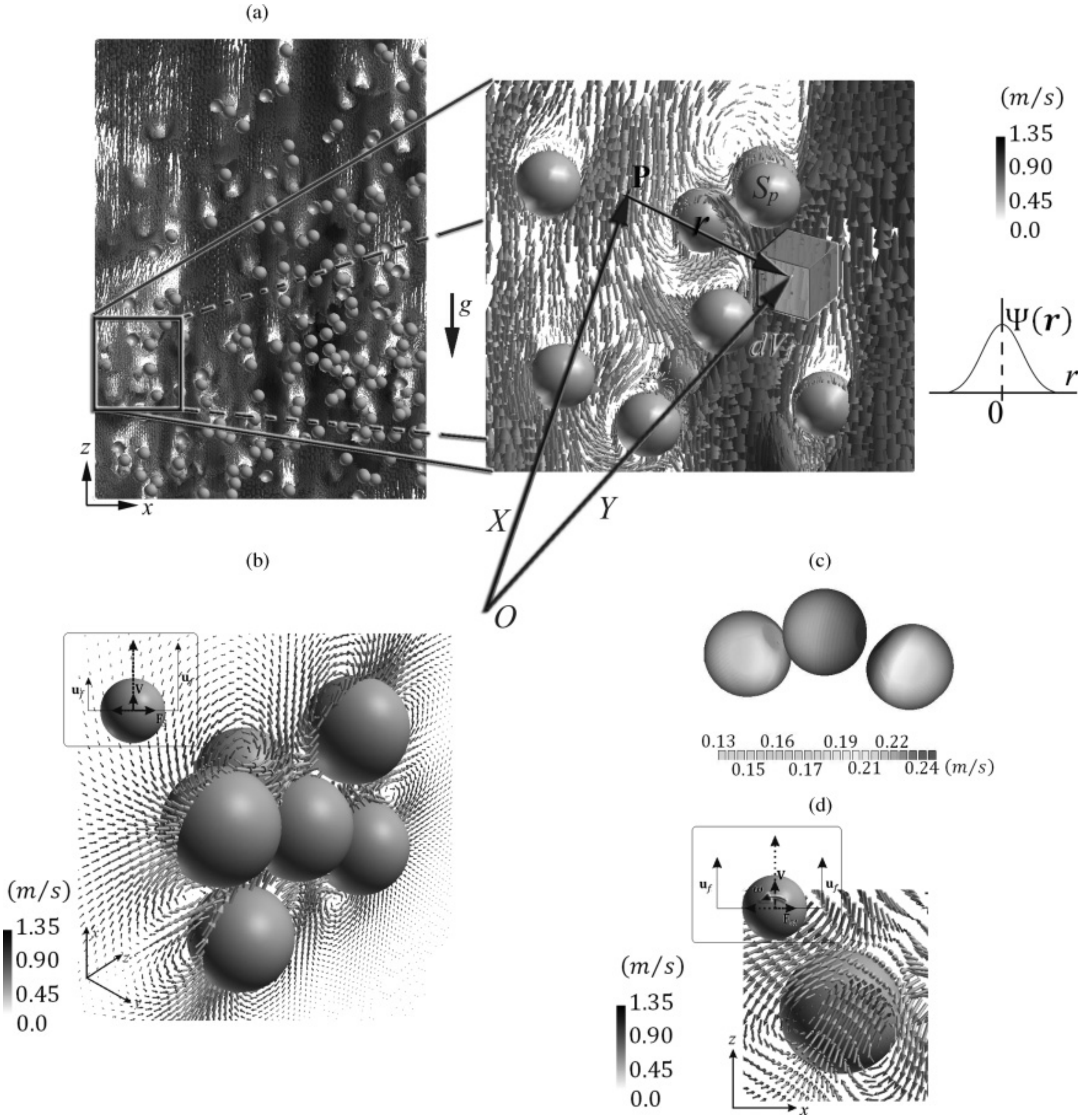

FIG. 6. (a) Computed instantaneous air flow field in an air-immersed granular bed under vibration on a cutting xz plane. Here, $\Gamma = 7.05$, $\omega/2\pi = 32$, $A = 0.17$ cm, and $H_0 = 4.2$ cm. Inset: The averaging region and typical shape of a weighting function. (b) Instantaneous coarse-mesh resolved air flow field for the case in (a). Inset: The direction of the Saffman lift. (c) Three beads from the middle of the broken chain in Fig. 4(e). Here, the deformations are exaggerated to highlight the shape of the contact area between the grains. (d) The Magnus lift induced by the grain rotation. Inset: Direction of the Magnus lift.

Lift forces are difficult to model, partly because collisions between beads cause them to rotate. Figure 6(c) illustrates three beads from the middle of the broken chain in Fig. 4(e). In Fig. 6(c), by use of gray-scale image coding, clear evidence is presented that the beads rotate. The deformations are exaggerated to highlight the shape of the contact area between the beads. The contact area is generally finite though small compared with the dimensions of the beads. Bead rotation generates a lift called the Magnus lift [27], whose direction is shown in the inset of Fig. 6(d). The Magnus lift, like the Saffman lift, may cause the beads in a chain to slip relative to each other.

In a two-phase system such as that depicted in the inset of Fig. 6(a), the dynamics of air should be completely described by the Navier-Stokes equations valid at each point within air. Here, the point variables such as density and velocity (which may vary rapidly on a scale comparable to the particle spacing) are replaced with smoothed variables obtained by averaging over volumes that are large compared to the interparticle spacing, but small compared to those characterizing the mean flow in the cell.

To define the average value at a point **P**, a weighting function, $\Psi(r)$, may be introduced. This function is positive for all r and smoothly decreases with increasing r such that derivatives of all orders exist. The local mean volume fraction of space occupied by air may be defined as

$$\phi_a(X,t) = \int_{V_f} \Psi(X - Y)\, dV_f, \tag{7}$$

where V_f represents all points $\boldsymbol{Y}$ occupied by air at time t, as shown in the inset of Fig. 6(a).

Air is assumed to be *incompressible*. Thus, velocity at all points instantaneously occupied by air satisfies the continuity equation in terms of local mean air properties, which may be obtained as

$$\frac{\partial \phi_a}{\partial t} + \nabla \cdot \phi_a \mathbf{u}_a = 0. \tag{8}$$

In a similar way, the averaged air-momentum balance may be obtained as

$$\rho_a \phi_a \left(\frac{\partial \mathbf{u}_a}{\partial t} + \mathbf{u}_a \cdot \nabla \mathbf{u}_a \right) = \nabla \cdot (\phi_a \mathbf{T}) + \mathbf{f}_{\text{ag}} + \rho_a \phi_a \mathbf{g}, \tag{9}$$

where $\mathbf{T}$ is the spatially averaged air stress tensor, $\mathbf{f}_{\text{ag}}$ is the air-grain interaction force per unit volume, ρ_a is the density of air, and $\mathbf{g}$ is the acceleration due to gravity. The air-grain interaction force per unit volume may be represented as [28]

$$\mathbf{f}_{\text{ag}} = (\mathbf{f}_D + \mathbf{f}_S + \mathbf{f}_M + \mathbf{f}_A + \mathbf{f}_s + \mathbf{f}_b + \mathbf{f}_B), \tag{10}$$

where $\mathbf{f}_D$, $\mathbf{f}_S$, $\mathbf{f}_M$, $\mathbf{f}_A$, $\mathbf{f}_s$, $\mathbf{f}_b$, and $\mathbf{f}_B$ represent the drag, Saffman, Magnus, added mass, stress, buoyancy, and Basset history forces per unit volume. The resulting equation (9) describes the motion of air when occupying the whole volume, resisted by its motion relative to the grains [10].

Existing literature on the flow of fluids through granular beds gives very limited information on the criteria for the transition from laminar to turbulent flow [29]. Kececioglu and Jiang have used a bed consisting of 3-mm grains [30]. They have observed Darcy's flow for $0.3 < \text{Re} < 0.7$, Forchheimer (laminar) flow for $1.6 < \text{Re} < 10.0$, and the turbulent regime for $13.0 < \text{Re} < 90$. Here, Re represents the Reynolds number based on the bead diameter, defined as $\text{Re} = \sigma u/\nu$, where ν is the kinematic viscosity of the fluid. The Reynolds number of the granular bed in Fig. 6(a) is approximately 35. Therefore, air is turbulent in Fig. 6(a). However, in the system as shown in Fig. 5(a), both turbulent and laminar regimes can exist. Researchers are faced with a significant challenge defining the conditions for the onset of turbulence in granular beds.

In the present attempt, large-eddy simulation (LES) techniques [9] are utilized to solve the modified Navier-Stokes equations (8) and (9), which include variables such as the local volume fraction.

C. Models for the granular phase

A force-driven model as described in Ref. [9] has been utilized to investigate the flow dynamics of granular flows in an intermediate regime, where both collisional and frictional interactions affect the flow behavior.

In brief, the aforementioned model describes how the typical ith grain translates and spins, depending on the forces and torques acting on it. In the presence of a *nonuniform* flow field of air, as illustrated in Fig. 6(a), the forces exerted by the air on the grains encompass the drag, lift, added mass, and Basset history forces [28]. The Basset history contribution is neglected in the present attempt. The added mass and buoyancy forces are important for liquid-solid suspension. Therefore, their contributions are neglected given the circumstances.

Here, two contributions to the torque acting on the ith grain are taken into account: the torque acting on the grain by neighboring grains caused by frictional contact forces in grain-grain interactions, and the resistive torque applied to the rotating grain due to air shear stress distribution on the grain surface.

The model described in Ref. [9] combines the Lagrangian (particle-based) and the Eulerian (grid-based) methods. A unification of solid body and fluid simulations is achieved in which each grain continuously interacts with every other grain and the fluid. This method requires a very large number of grains to produce realistic results. The advantage of this model is that *real-world applications over long simulation runs* of 10^9 time steps can easily be performed. However, a number of empirical expressions are used. In addition, there exist controversies over issues such as the form of dependence of subgrid scale viscosity on the resolved rate of strain tensor. Sundaresan [31] suggested that subgrid scale viscosity is inversely proportional to the rate of strain in turbulent beds. This is a controversial issue. The identification and rationalization of scaling requires fresh thinking.

To develop accurate models for the SGS stress tensor, the effects of unresolved structures should be taken into account. It is worth mentioning that systems like the one shown in Fig. 2 are too opaque to permit nonintrusive optical measurements. The other nonintrusive measurement techniques, such as capacitance, impedance and γ-ray tomographies, and radioactive particle tracking, do not produce adequate resolution for developing subgrid models. Subgrid-scale fluid structures in systems like the one illustrated in Fig. 2(d) arise because of local instability, and chainlike structures are known [32] to contribute to energy removal from the resolved scales of air. These coupling effects might be modeled by superposing particle-induced SGS energy dissipation to that induced by shear [33].

The VMS uses a few empirical constants including the exponential decay coefficient in Eq. (1). However, real-world applications using VMS over long simulation runs will remain intractable in the foreseeable future. Accurate numerical resolution often demands impractically difficult computations.

IV. RESULTS AND DISCUSSION

A. Model validation

To assess the quality of the model described in the preceding section, the flow of a dense granular media immersed in air was simulated using a large number of identical rough glass beads with diameter $\sigma = 330$ μm in the cell, as shown in Fig. 1(b). The cell was initially filled up to the level free surface at $h = 4.2$ cm. The physical and mechanical properties of the beads are given in Table I. The physical properties of air are given in Table II. The free surface was flat before the oscillations were started. The initial average solid fraction

TABLE II. Physical properties of air.

Physical Properties	
Density	1.2 kg/m^3
Dynamic viscosity	1.82×10^{-5} kg m/s
Temperature	293 K

was $\overline{\phi_s} = 0.55$ and the friction coefficients between the beads were estimated using Eq. (1). The effect of surface friction is approximated by a restoring, tangential force that counteracts mutual sliding motion at contact [7].

Assuming sinusoidal oscillations for the cell, $z = A\sin(\omega t)$, simulations are performed at seven different oscillation frequencies. They are $\omega/2\pi = 17.1$, 19.1, 30.8, 33.1, 35.6, 39.18, and 40.1, respectively. The gravitational constant is $g = 9.81$ m/s^2 and $A = 0.17$ cm. Thus the aforementioned frequencies correspond to $\Gamma = 2$, 2.5, 6.5, 7.5, 8.68, 10.5, and 11, respectively.

To obtain numerical solutions of Eqs. (8) and (9), the solid volume fraction at the appropriate grid nodes must be specified. The value of solid volume fraction is obtained from molecular-dynamics simulations by counting the volume of grains within each computational cell divided by the cell volume. The governing equations are fully solved with a second-order finite volume method on a staggered grid. The central differencing scheme is used for spatial discretization and the time is advanced via a second-order implicit scheme. In addition, the equations of motion of the grains [9] are integrated on a step-by-step basis using the Verlet algorithm [22] by applying a time step $\delta t = 10^{-8}$s, which equals the time step for solving Eqs. (8) and (9) for the gaseous phase. The no-slip boundary condition is applied on the surfaces of the container. Furthermore, it is assumed that the top surface of the container is open to the atmosphere, namely $p|_{z=H_{\mathrm{vout}}} \approx p_{\mathrm{atm}}$.

In the following sections, the data obtained from the simulations of grains when subjected to vertical vibration in the presence of air will be analyzed. The aim is to explore the interplay between granular separation and the cyclic motion of air through the bed.

1. Faraday tilting

Faraday [4] has suggested that air strongly influences the motion of fine grains that vibrate vertically. In this case, air pockets are being driven back and forth through the bed by the vibration [34], which could cause heaps to form spontaneously.

In qualitative agreement with the Faraday experiment, Fig. 7(a) shows the spontaneous tilting of collections of fine grains vibrated vertically in the cell. The tilt angle given approximately as $\tan^{-1}[(H_h - H_l)/2(R_0 + t)]$ ranges between a dynamic angle of repose, θ_d, and a maximum angle of stability. The angle is maintained by the balance between the bulk tilt enhancement early in flight and the bulk tilt detractions caused by landing and surface grains cascading down the upper slop [3]. The inclined solid line in Fig. 7(a) represents the heap slop in the experiment. The heap slop in the simulation shows reasonable agreement with the experiment. Here, $\Gamma = 2$, $\omega/2\pi = 17.1$, $A = 0.17$ cm, and $H_0 = 3.2$ cm. In this simulation, the initial bed height is shorter than that use in Fig. 1(a). Note that simulations of 5×10^5 grains at low-frequency vibrations over long simulation runs of 10^{10} time steps are quite expensive. In addition, an accurate numerical resolution can be achieved using a shorter bed, as illustrated in Figs. 7(a) and 7(b).

As frequency increases, the Faraday tilting effect is expected to become weaker. Figure 7(b) is a snapshot of the simulation at $\Gamma = 2.5$, $\omega/2\pi = 19.1$, $A = 0.17$ cm, and $H_0 = 3.2$ cm. The tilt angle is smaller than that shown in Fig. 7(a). Granular media in Figs. 7(a) and 7(b) can exhibit properties of both liquids and solids. At the lower frequency of 17.1, the regime in the bulk bed is strongly rate-independent intermittent, for which a uniform rescaling of the strain rates leave the stress unchanged. The bed dynamics become more continuous at the higher frequency of 19.1.

Figure 7(c) illustrates a snapshot of the experimental cell in which the fine grains are being vertically vibrated at the experimental parameter values: $\Gamma = 2.5$, $\omega/2\pi = 19.1$, and $A = 0.17$ cm. The initial bed height is the same as in the simulation, namely 3.2 cm.

As can be seen from Fig. 7(b), the grains on the left side of the cell close to the walls get pushed up, while the right side cascades down onto the left side. Although a remarkably good agreement exists between simulations and experiments concerning this feature, the simulations are found to slightly overpredict the tilt angle. The experimental results indicate that the fluid-grain coupling weakens if the frequency is raised. One aspect that bears on the adequacy of the model is the description of the fluid-grain drag. Note that the use of the Ergun bed equation [35] instead of the empirical formula of Wen and Yu [36] might slightly improve the simulation results. Accurate predictions can be achieved using the VMS, which does not use any empirical bed equation, and it is valid in both dense and dilute regimes. However, simulations of 10^5 grains over long simulation runs of 10^{10} time steps are quite time-consuming.

Figure 7(d) shows the single-grain velocity distribution functions (VDF's) sampled at sampling ports "SP1" in Figs. 7(a) and 7(b). Circles and squares represent VDF's of samples taken from Figs. 7(a) and 7(b), respectively. As can be seen from Fig. 7(d), the VDF's are near Gaussian but anisotropic. This indicates that the grains that cascade down the outer surface of Faraday piles do not have any local equilibrium.

Figure 7(e) illustrates the VDF of a sample taken at sampling port "SP2" in Fig. 7(a). As can be seen from Fig. 7(e), the VDF is non-Gaussian describing the collective intermittency because of grain correlations during each static state. The flow at sampling port "SP2" is due to rubbing contact of slowly driven grains in a near-packed arrangement.

2. Bubbling in granular films

Another phenomenon observed in vertically vibrated granular materials is *bubbling* [2]. The onset of bubbling may be related to a qualitative change in the flow. Figure 7(b) shows convective rolls from the lower part of the bed toward the upper part. Pak and Behringer [2] have speculated that convective motion near the upper part of the bed reverses, and that the grains flow down in the center. They have also suggested that bubbles form because compressed air trapped in the granular material expands when the grains leave the shaker base and they are in free flight [2]. Fluid-immersed beds under vibration are complex, and considerable insight may be gained from computer simulations.

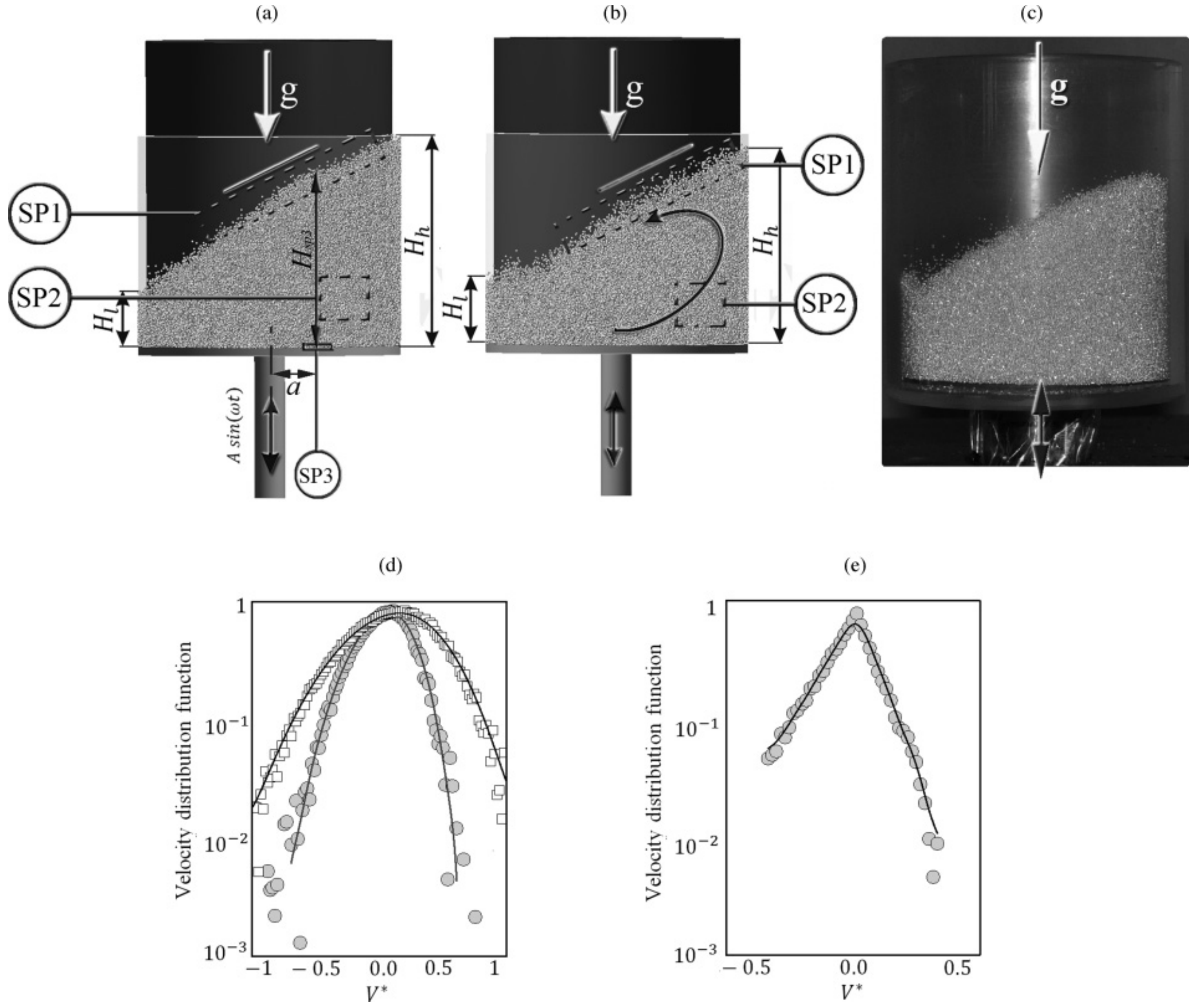

FIG. 7. (a) Computed spontaneous tilting of collections of fine grains vibrated vertically in the cell. Here, $\Gamma = 2$, $\omega/2\pi = 17.1$, $A = 0.17$ cm, and $H_0 = 3.2$ cm. (b) Snapshot of the simulation at $\Gamma = 2.5$, $\omega/2\pi = 19.1$, $A = 0.17$ cm, and $H_0 = 3.2$ cm. (c) An image of the experimental cell. The grains are being vertically vibrated at $\Gamma = 2.5$, $\omega/2\pi = 19.1$, and $A = 0.17$ cm. The initial bed height is 3.2 cm. (d) The grain velocity distribution functions (VDF's) sampled at sampling ports "SP1" in (a) and (b). Circles and squares represent VDF's of samples taken from (a) and (b), respectively. (e) The VDF of a sample taken at a sampling port "SP2" in (a).

As stated earlier, the computer simulations of Ref. [2] require more than 10^7 grains. An accurate numerical resolution of a system with 10^7 grains demands huge computational resources. In addition, useful methods such as digital image processing (DIP) [8] cannot be effectively used to discern the surface fraction of voids and chain-size distribution. Careful visual inspection of Fig. 2(a) in Ref. [2] reveals that a bubble has decreased very much in size when it reaches the free surface, as illustrated in Fig. 2(b) [2]. This suggests that the bubbles in Ref. [2] are not likely to be two-dimensional. Therefore, the results reported in Fig. 3 in Ref. [3] should be accepted with caution.

In light of the above discussion, it will be advantageous to investigate bubbling in vertically vibrated granular films. The experimental results are reported in Sec. II. The current section will report on computer simulations of bubbling in granular films that were performed using fewer than 10^5 grains.

The main objective is to verify the validity of the model. To achieve this, the experimental results reported in Sec. II will be compared with the results of the simulation. Figure 8(a) is an enhanced version of Fig. 2(b), made to help identify individual grains. This image is used to compute statistics for the grains in the cell, including the chain-size distribution. In Fig. 2(b), the background illumination is nonuniform. A morphological image processing [8] is applied to estimate the background illumination. This step is followed by dilation to remove objects that cannot completely contain the structuring element. Figure 8(a) is a binary image with a uniform background. It can be conveniently used to find all the connected grains and to calculate the surface fraction of voids. This method can also be used to measure the displacement of grains by analyzing sequences of images of the cell taken with a charge-coupled device (CCD) camera.

A drawback of the aforementioned method is that the gap of the experimental cell is approximately six grain diameters. In this circumstance, in a two-dimensional (2D) image such as Fig. 2(b), there will be a number of overlaps between grains from different layers. Obviously, 2D projected images

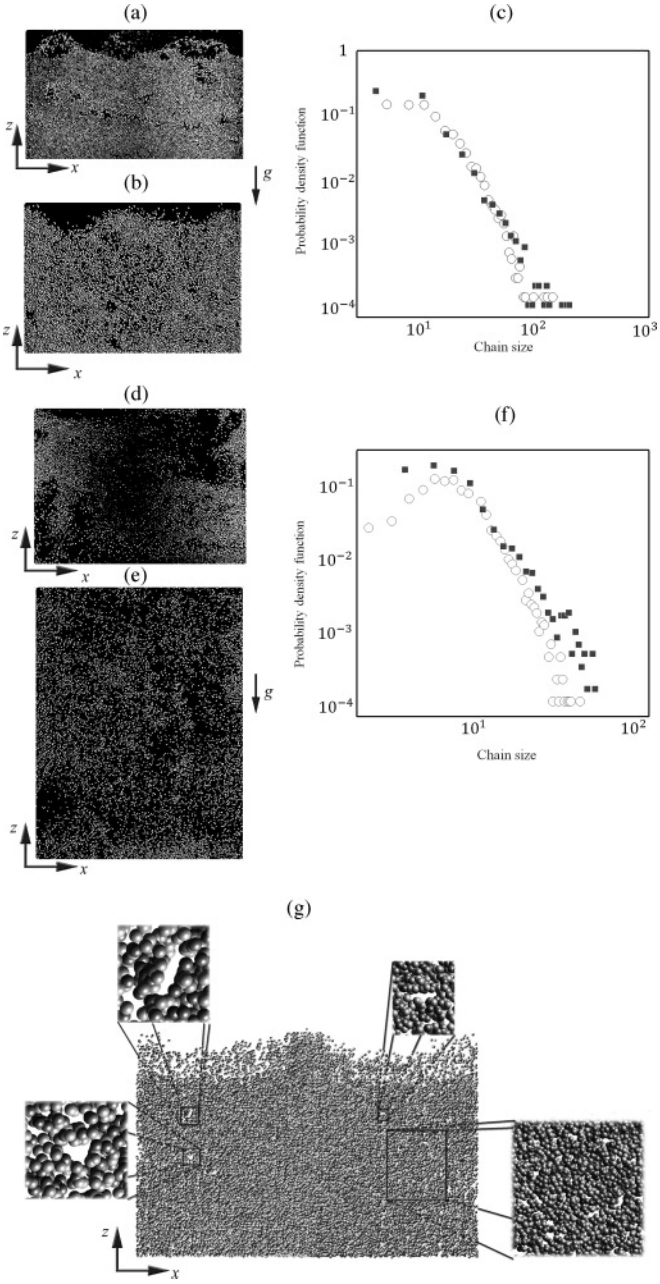

FIG. 8. (a) An enhanced version of Fig. 2(b). (b) An enhanced snapshot of the simulation. Here, $\Gamma = 6.5$, $\omega/2\pi = 30.8$, $A = 0.17$ cm, and $H_0 = 4.2$ cm. (c) The probability distribution function of chains in the cell. Squares and circles represent the PDF's of the experiment and the simulation, respectively. (d) and (e) Snapshots of the experiment and the simulation, respectively, at $\Gamma = 11$, $\omega/2\pi = 40.1$, $A = 0.17$ cm, and $H_0 = 4.2$ cm. (f) The comparisons of the PDF's from experiment and simulation. (g) Image of grains with diameter $\sigma = 1200$ μm in a vertically vibrated shaker on an xz-plane at $t = 1.02$ s. The simulation parameter values are $\Gamma = 6.5$, $\omega/2\pi = 30.8$, $A = 0.17$ cm, and $H_0 = 7.3$ cm. The container is a thin annular with inner diameter $D = 17$ cm and a radial gap size of $t = 0.7$ cm.

cannot be used to determine the 3D granular structures in the experimental cell. Of particular interest is the relationship between coherent 2D granular structures determined using the aforementioned image-processing technique and the structures in 3D space. In the present implementation, it is only possible to determine the likelihood that the 2D structures can be found in the experimental cell. An extension would be to utilize computer-simulation results to improve the prediction of image-processing methods. The subject appears to be encouraging enough to merit further investigation.

Figure 8(b) illustrates an enhanced snapshot of the simulation. Here, $\Gamma = 6.5$, $\omega/2\pi = 30.8$, $A = 0.17$ cm, and $H_0 = 4.2$ cm. Figure 8(c) depicts the probability distribution function of chains in the cell. Squares and circles represent the PDF's of the experiment and the simulation, respectively. It can be seen that the simulation results nearly coincide with the experimental results. In addition, the void surface fractions in Figs. 8(a) and 8(b) are nearly the same.

The second test is to assess the ability of the model to predict turbulent granular films. Figures 8(d) and 8(e) illustrate snapshots of the experiment and the simulation, respectively, at $\Gamma = 11$, $\omega/2\pi = 40.1$, $A = 0.17$ cm, and $H_0 = 4.2$ cm. The comparisons of the PDF's from experiment and simulation are displayed in Fig. 8(f). Here, squares and circles represent the results from experiment and simulation, respectively. The results confirm the earlier agreement between simulation and experiment. The model is therefore deemed to be sufficiently flexible to capture a number of salient features of experiments with fluid-immersed granular beds subject to sinusoidal vertical vibration.

Figure 8(g) shows the instantaneous configuration of grains with diameter $\sigma = 1200$ μm on an xz plane at $t = 1.02$ s. The grains are vibrated vertically in the computational cell at the simulation parameter values $\Gamma = 6.5$, $\omega/2\pi = 30.8$, $A = 0.17$ cm, and $H_0 = 7.3$ cm. In this case, the container is a thin annular with an inner diameter $D = 17$ cm and a radial gap size of $t = 0.7$ cm. As can be seen from Fig. 8(g), the trapped air inside the granular assembly can escape more easily through the interstitial between grains without significant

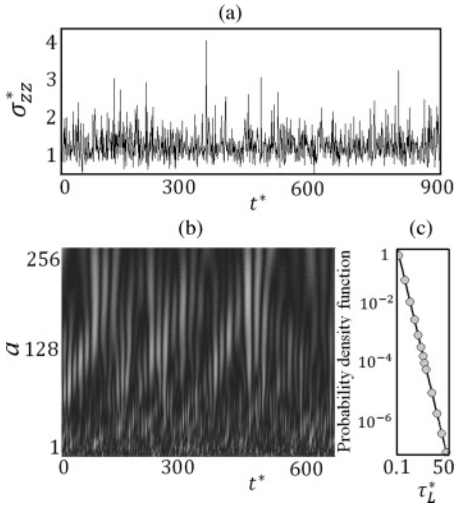

FIG. 9. (a) Typical time series for the normalized normal stress σ^*_{zz} as a function of dimensionless time, $t^* = t\omega/2\pi$, at the sampling port "SP3" in Fig. 7(a). (b) The continuous wavelet transform (CWT) of the time series in (a) vs scale a. (c) The PDF of the filtered data. The PDF reveals a power-law behavior of the waiting times, $P(\tau_L)\tilde{\tau}_L^{-\alpha}$ with $\alpha = 2.2$.

bubbling behavior. Therefore, the bubbling behavior would be expected to stop entirely with large enough particles.

B. Spatiotemporal fluctuations in a dense slowly evolving granular system

In this section, a quantitative step is taken toward a further understanding of spatiotemporal fluctuations in dense granular flows. Figure 9(a) illustrates typical time series for the normalized normal stress σ_{zz}^*, calculated using Eq. (2), as a function of dimensionless time, $t^* = t\omega/2\pi$, at the sampling port "SP3" as shown in Fig. 7(a). The data are normalized by the average hydrostatic pressure, defined as $[(1-\overline{\phi_a})\rho_p + \overline{\phi_a}\,\rho_a]g\,\overline{H_{sp3}}$, at the sampling port whose active area is 10 mm^2.

In a dense granular flow, an increase of fluctuations relative to the average as shown in Fig. 9(a) may cause jamming of slowly driven grains. Such granular jams form very quickly. It requires a significant time and energy transfer for a jammed system to start moving again. It is instructive to investigate the distribution of waiting times, namely, the time intervals between two successive bursts of dissipation in the time series in Fig. 9(a). A burst of dissipation is defined by the condition $\sigma_{zz}^*(t^*) \geqslant \overline{\sigma_{zz}^*} + 2S_\sigma$, where S_σ is the standard deviation of the time intervals between the bursts. This definition is used to calculate the distribution functions for the peak values of bursts.

The statistics of the waiting times give an idea of the dynamic behavior of the system. A wavelet transform method [37] is used to separate burst periods from waiting times, τ_L. The continuous wavelet transform (CWT) of the time series in Fig. 9(a) versus scale a using a symlet 7 proposed by Daubechies [37] is shown in Fig. 9(b). The probability density function (PDF) of the filtered data is shown in Fig. 9(c). As can be seen from Fig. 9(c), the waiting time distribution (of approximately 45 s of simulation results) reveals some correlations between successive bursts that cannot be attributed to a nonstationary Poisson distribution. On the contrary, an analysis of the PDF reveals a power-law behavior of the waiting times, $P(\tau_L)\tilde{\tau}_L^{-\alpha}$ with $\alpha = 2.2$, indicating a correlation between successive bursts of dissipation. The exact value of the exponent is affected by the length of the observation (simulation) time. However, the observation time

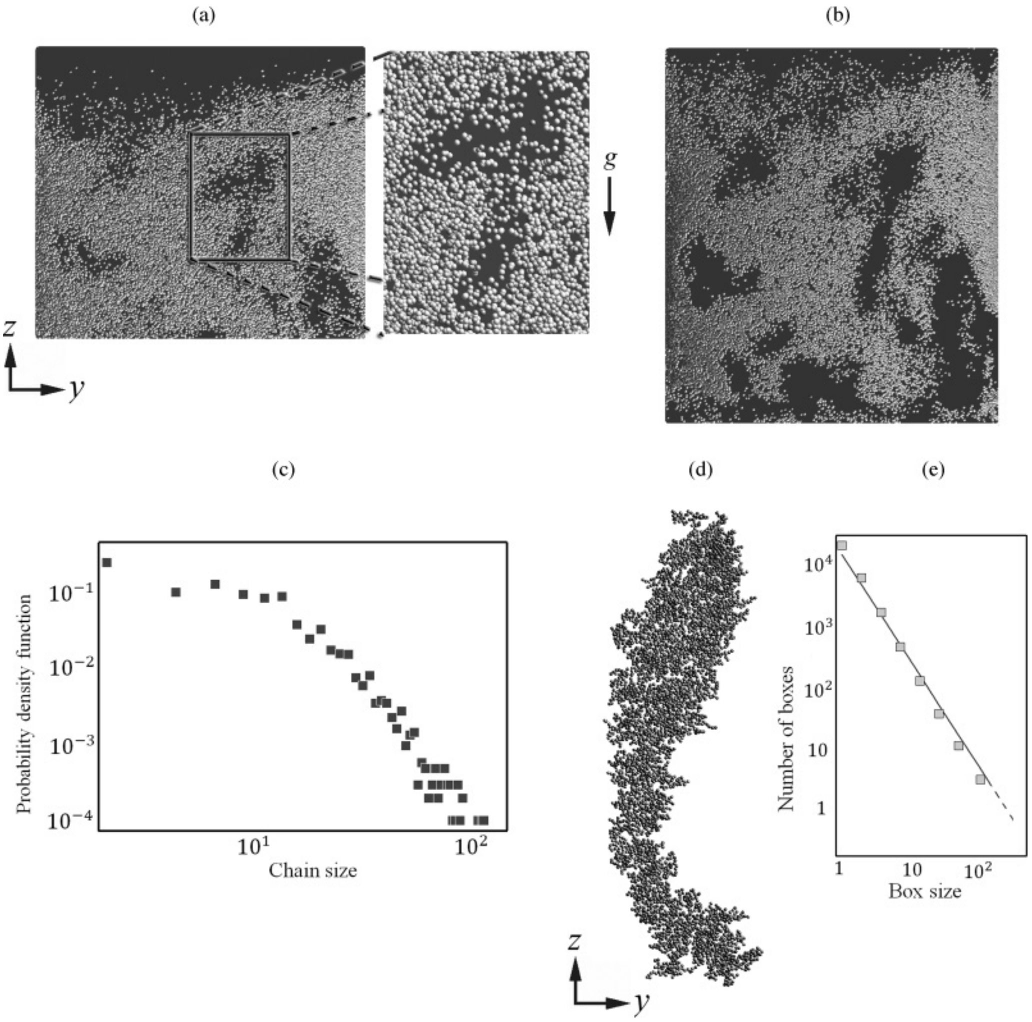

FIG. 10. (a) A snapshot of a fingerlike branching pattern at $\Gamma = 8.68$, $\omega/2\pi = 35.6$, $A = 0.17$ cm, and $H_0 = 4.2$ cm. Inset: The magnified pattern. (b) A snapshot of simulation taken $t = 0.08$ s after the snapshot in (a). (c) The probability density function of chains vs chain size for the granular assembly in (b). (d) A typical large chain in (b). (e) Number of boxes of size R needed to cover the chain. Here, the fractal scales as $R^{1.75}$.

does not seem to be sufficiently long that the power-law distribution of waiting times can be considered to be firmly established.

In brief, in the system illustrated in Fig. 7(a), the dissipative events are suddenly distributed in time and the dynamics appears to be chaotic.

C. Fractal structures in the grain-gas interface

Pak and Behringer [2] have observed that large bubbles can exhibit a characteristic fingerlike structure inside the bubble. In this section, the validated model is employed to investigate granular fingering instability. Figure 10(a) depicts a fingerlike branching pattern at $\Gamma = 8.68$, $\omega/2\pi = 35.6$, $A = 0.17$ cm, and $H_0 = 4.2$ cm. The pattern is magnified and replotted in the inset.

Figure 10(b) illustrates the granular fingerlike structures at a later stage. The snapshots in Figs. 10(a) and 10(b) are separated by $t = 0.08$ s. Figure 10(c) illustrates the probability density function of chains versus chain size for the granular assembly shown in Fig. 10(b). It is not quite obvious that the distribution in Fig. 10(c) is a Schulz distribution. However, the approach described in Sec. III A can be used to estimate the shear viscosity of the system in Fig. 10(b). Granular fingering instability merits further investigation.

Visual inspection of Fig. 10 reveals that the grain-air interfaces exhibit fractal-like structure. To quantify the fractal dimension of the chainlike structures, the box-counting method, D_{2d}, detailed in Sec. III is used. This denotes 2D characteristic of the grain-air interfaces. More than 25 representative images of the grain-air interface such as that shown in Fig. 10(d) are used. Figure 10(e) illustrates the number of boxes of size R needed to cover the chain. In Fig. 10(e), a solid line is fitted whose slope is 1.75. Note that the fractal-like structure in Fig. 10(d) holds its fractality over nearly three orders of magnitude.

The fractal dimension of the fingerlike branching patterns in Fig. 10 is $D = 1.7 \pm 0.05$. The fingering pattern found here appears to be different from viscous fingering, which only happens in a Hele-Shaw geometry. However, these two phenomena may be remotely related.

D. Turbulent granular films

When Γ increases much above Γ_b, a novel bubbleless behavior similar to turbulent fluidized beds [38,39] is observed. Figure 11(a) depicts an example snapshot of a turbulent-like fluidization at $\Gamma = 10.5$, $\omega/2\pi = 39.18$, $A = 0.17$ cm, and $H_0 = 4.2$ cm. In this case, the particles aggregate into chains to make way for rapid air flow. In a turbulent fluidization, the chains frequently dissolve and reform with fresh grain members with consequent high rates of air-grain mass and heat transfer [39]. These are hardly realizable with bubbling fluidization.

For beds with vertically vibrated granular materials in the turbulent regime with $\Gamma > 10$, experiments may be very difficult to carry out while computer simulations would be perfectly feasible. Note that turbulent fluidized bed reactors are widely used in the petrochemical industry, coal combustion, and calcining processes.

Figure 11(b) shows a typical snapshot from a simulation with $\Gamma = 11$, $\omega/2\pi = 40.1$, $A = 0.17$ cm, and $H_0 = 4.2$ cm. Vigorous solid mixing carries the chain-size distribution through a transient or temporal stage until a steady state is achieved. A typical PDF from the simulation is displayed in Fig. 8(f). Although the distribution functions are path-dependent, the chain-size distribution remains closely related to the Schulz distribution up to and including steady state. In this case, a kinetic-type theory can be developed for the polydisperse chains mixture to predict the behavior of turbulent beds of grains successfully. As stated earlier, a presentation of the full theory is beyond the scope of this work and will be taken up elsewhere.

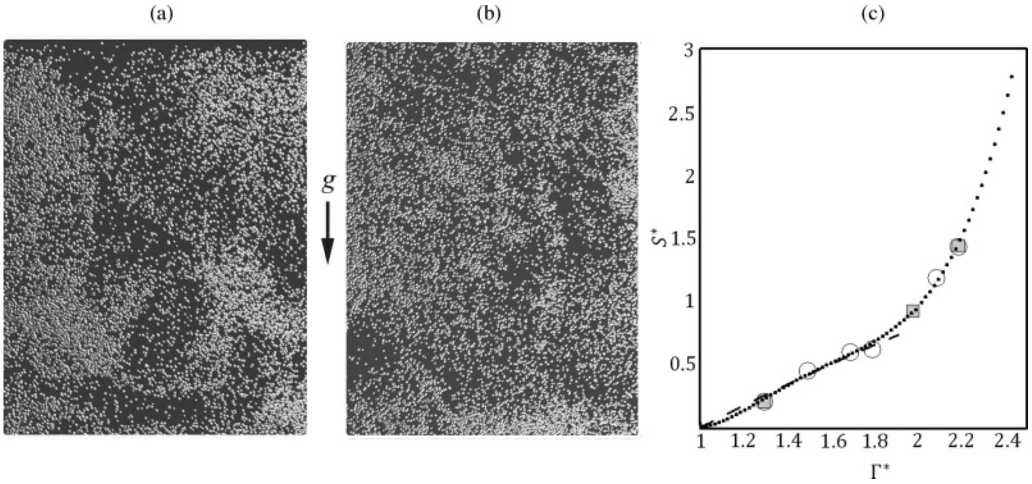

FIG. 11. (a) A snapshot of a turbulent-like fluidization at $\Gamma = 10.5$, $\omega/2\pi = 39.18$, $A = 0.17$ cm, and $H_0 = 4.2$ cm. (b) A typical snapshot from a simulation with $\Gamma = 11$, $\omega/2\pi = 40.1$, $A = 0.17$ cm, and $H_0 = 4.2$ cm. (c) The normalized void area, S^*, as a function of Γ^*. The dotted line is a fit whose expression is given in the text. Circles and squares represent the simulation and the experimental results, respectively. The dashed line is similar to the correlation presented in Ref. [2].

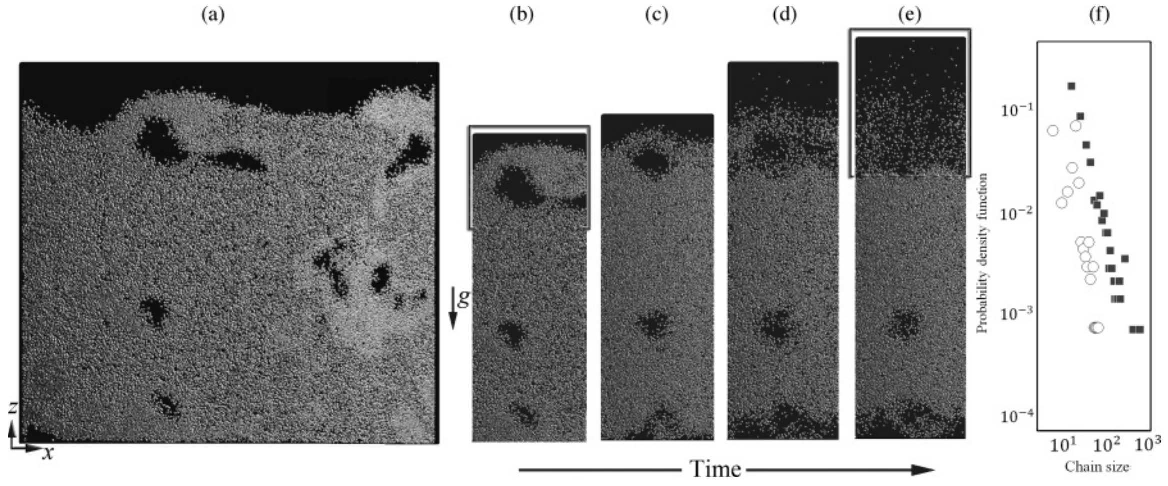

FIG. 12. (a) A snapshot from a simulation with $\Gamma = 7.5$, $\omega/2\pi = 33.1$, $A = 0.17$ cm, and $H_0 = 4.2$ cm. (b)–(e) A sequence of snapshots each separated by $t = 0.02$ s capturing bubble dynamics in a narrow section of the cell. (c) Comparisons of the PDF's of the chain size distributions in the framed area in the upper part of (b) and (e). Squares and circles represent the PDF's for (b) and (e), respectively.

Figure 11(c) illustrates the normalized void area, S^*, defined as S/H_0C, as a function of $\Gamma^* = \Gamma/\Gamma_b$. Here C is the circumference of the cell. Squares and circles represent the results from the experiment and the simulation, respectively. The dotted line is fitted by

$$S^* = -5.26 \times 10^2 e^{-0.04/\Gamma^*} - 5 \times 10^2 e^{-0.02/\Gamma^*} + 1.82 \times 10\Gamma^* - 4.03\Gamma^{*3} + 1.08\Gamma^{*4}. \qquad (11)$$

The expression of Eq. (11) is an Arrhenius-type. This correlation has superior performance over its predecessor presented in Ref. [2] because a transition from bubbling to turbulent bed (in which the state becomes more disordered and spatial homogeneity may be recovered) can be predicted at high Γ. The dashed line is similar to the correlation presented in Pak and Behringer [2].

E. From formation of a bubble to its burst

The life of a single bubble may be summarized as occurring in the following phases: nucleation, growth, and collapse. Figure 12(a) shows a snapshot from a simulation with $\Gamma = 7.5$, $\omega/2\pi = 33.1$, $A = 0.17$ cm, and $H_0 = 4.2$ cm. As can be seen from Fig. 12(a), there are at least nine large bubbles in the vertically vibrated granular film whose average thickness is less than 10 grains. The regions characterized by highly non-Gaussian fluctuations with close to t distributions are slightly lighter in Fig. 12(a). There is a close relationship between the deviation from Gaussian distribution and the local solid volume fraction. Obviously, semiphenomenological approaches based on the application of the Enskog-Boltzmann equation [24] are not suitable for modeling the solid phase in the bubbly regime. However, they can be used to model the polydisperse mixture of chains found in turbulent granular films.

The nucleation of bubbles is of particular interest. Pak and Behringer [2] have observed that bubbles do not form during the part of the cycle when air is forced into the granular assembly from the bottom. During the cycle when the grains leave the base, small cavities are formed due to the mesoscale process resulting from a local pressure reduction such as occurs in accelerated flow. The primary requirement for nucleation to occur is that the granular assembly be agitated.

Figures 12(b)–12(e) show a sequence of snapshots each separated by $t = 0.02$ s capturing bubble dynamics in a narrow section of the cell. A waiting period occurs in a bubble site just after the departure of a bubble and before a new bubble is formed. The bubbles depart and move upward.

A complex air motion in the bed is initiated and maintained by the nucleation, growth, departure, and collapse of bubbles, and by convection, as depicted in Fig. 13. The growth rate is small at first but increases at a later stage. While rising as the result of buoyancy, they contract and expand during each shaker cycle. This feature can clearly be seen from Figs. 12(b)–12(e). The growth process appears to be controlled by the rate of energy transferred from the air, yielding surrounding chainlike structures at the bubble interface. Fingerlike branching patterns can be observed at the grain-air interfaces in Fig. 12.

If the bubble contacts the free surface, it bursts, creating a spray of grains as shown in Fig. 12(e). Comparisons of the PDF's of the chain-size distributions in the upper part of Figs. 12(b) and 12(e) are displayed in Fig. 12(f). As can be seen from Fig. 12(f), the large chains keeping the air trapped in (b) have already been destroyed in (e) to make way for rapid air flow, as shown in Fig. 13(g). The complex air motion in the jetlike [40] granular spray is depicted in Fig. 13(h). Figure 13(i) reveals that the chain-size distribution is a Schulz distribution. Here, circles and squares represent the PDF's at two transient stages separated by $t = 0.005$ s. Figure 13(b) depicts a snapshot from the simulation before the collapse. Figure 13(c) depicts the contours of air pressure within a bubble. A more accurate numerical resolution can be obtained using the mesh-free version of the VMS, which uses a few empirical constants. However, the technique mentioned earlier

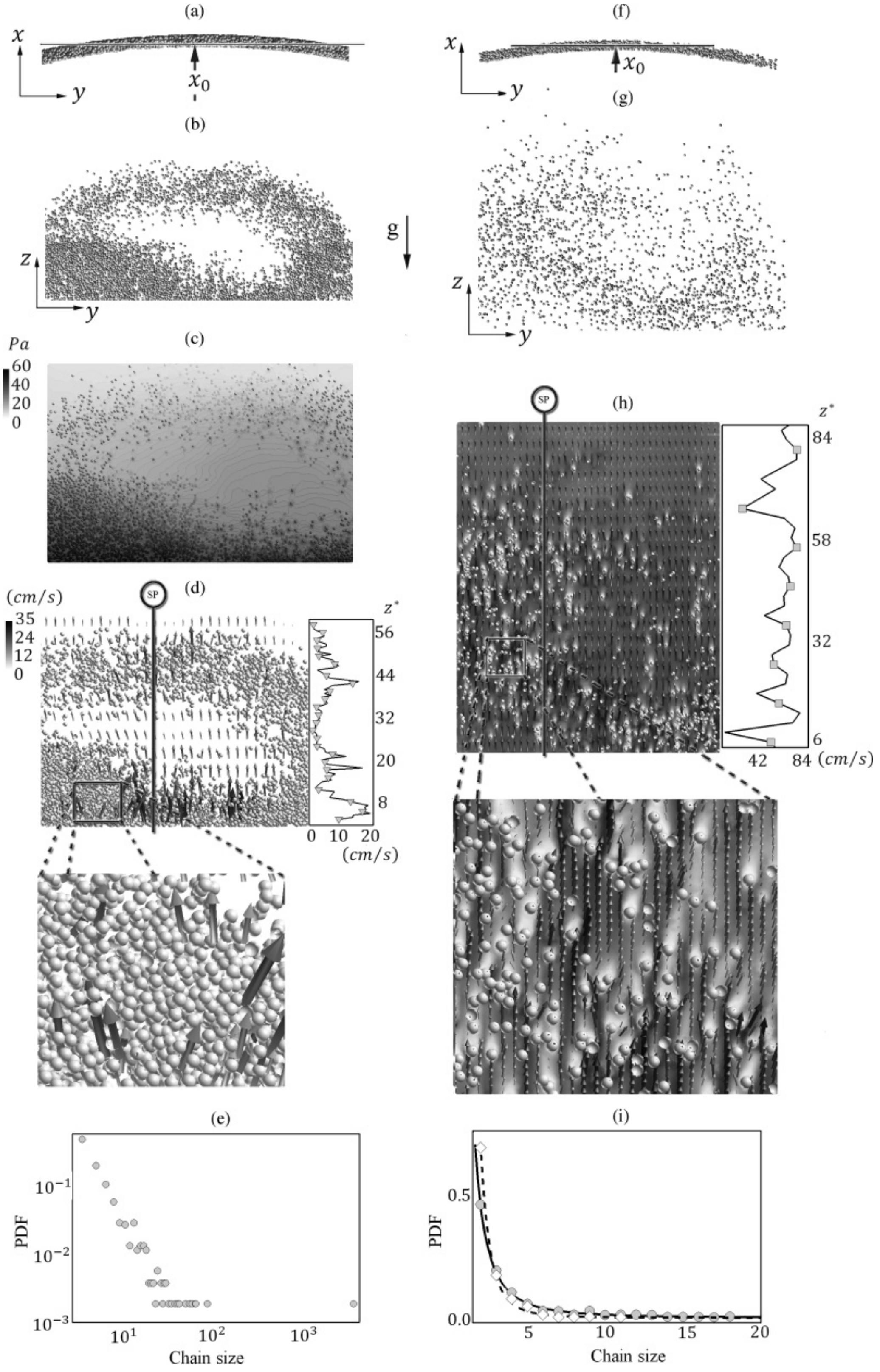

FIG. 13. (a) A Top view of grain in the cell. (b) A snapshot of a cavity on the cutting *yz* plane shown in (a) using a solid line. (c) Computed air pressure contours within the cavity in (b). (d) Computed (coarse mesh) instantaneous air velocity field within the cavity in (b). Inset: The magnified computed velocity vectors in (d). (e) The PDF of chainlike structures in the ensemble in (b). (f) A top view of grain in the cell after bubble bursting. (g) A snapshot of the jetlike spray on the cutting *yz* plane shown in (f) using a solid line. (h) Computed (coarse mesh) instantaneous air velocity field within the spray in (g). Inset: the magnified computed velocity vectors in (h). (i) The chain size distribution for lengths up to 20 grains in the spray in (g). Here, $\Gamma = 7.5$, $\omega/2\pi = 33.1$, $A = 0.17$ cm, $x_0 = 2.77$, and $H_0 = 4.2$ cm.

will be used to simulate stirred suspensions of nonspherical particles in a future paper.

V. CONCLUSIONS

Existing works on shaken sand have been largely confined to the experimental front using a huge number of grains. Unfortunately, this means that simulating these experiments, like the one described in Ref. [2], with accurate numerical resolution requires impractically difficult computations.

In this effort, experiments with vertically vibrated granular thin films with fewer than 10^5 grains were performed. In addition, computer simulations and theoretical investigations were carried out to develop a model of the flow dynamics of dense granular media immersed in air in an intermediate regime where both collisional and frictional interactions affect the flow behavior. The model was found to be sufficiently flexible to capture a number of salient features of the experiments, from Faraday tilting to bubbling and turbulent granular films.

The main finding is that the air-grain interfaces of bubblelike structures are found to exhibit a fractal structure with dimension $D = 1.7 \pm 0.05$.

More accurate numerical methods were introduced, namely a mesh-free version of the VMS. This technique will be used to simulate a dense, stirred suspension of nonspherical grains, the collision detection for which requires time-consuming computations.

On the theoretical front, it was suggested that a kinetic-type theory can be useful for modeling a polydisperse mixture of chains in turbulent beds. A presentation of the full theory will be taken up elsewhere.

ACKNOWLEDGMENTS

The author is grateful to Hrafn Arnórsson and Jun Huang for their careful review of this manuscript and suggestions for many revisions, and Vilhjálmur Sigurjónsson for his technical assistance.

---

[1] P. Umbanhowar, F. Melo, and H. Swinney, Nature (London) **382**, 793 (1996).

[2] H. P. Pak and P. R. Behringer, Nature (London) **371**, 231 (1994).

[3] P. J. King, P. Lopez-Alcaraz, H. A. Pacheco-Martinez, C. P. Clement, A. J. Smith, and M. R. Swift, Eur. Phys. J. E **22**, 219 (2007); The ratio of fluid drag forces to the grain inertial forces is a dimensionless number. However, the parameter $\nu/\beta\delta^2$ introduced on p. 220 of Ref. [3] is not dimensionless. It might be better to use the Stokes number instead.

[4] M. Faraday, Philos. Trans. R. Soc. London **121**, 299 (1831).

[5] X. Cheng, L. Xu, A. Patterson, H. M. Jaeger, and S. R. Nagel, Nat. Phys. **4**, 234 (2008).

[6] T. J. R. Huges, A. A. Oberai, and L. Mazzei, Phys. Fluids **13**, 1784 (2001); S. S. Collis, *ibid.* **13**, 1800 (2001); A. W. Verman, *ibid.* **15**, L61 (2003); A. Jafari, P. Zamankhan, S. M. Mousavi, and K. Hentinen, J. Appl. Phys. **100**, 034901 (2006).

[7] P. Zamankhan, Phys. Fluids **21**, 043301 (2009).

[8] R. C. Gonzales and R. E. Woods, *Digital Image Processing* (Addison-Wesley, Reading, PA, 1992).

[9] P. Zamankhan, Physica A **390**, 1402 (2011).

[10] D. Kunii and O. Levenspiel, *Fluidization Engineering*,1st Ed., (John Wiley and Sons, Inc., 1969); R. Jackson, *The Dynamics of Fluidized Particles* (Cambridge University Press, Cambridge, 2000).

[11] M. E. Cates, J. P. Wittmer, J.-P. Bouchaud, and P. Claudin, Phys. Rev. Lett. **81**, 1841 (1998).

[12] C. Ancey, J. Non-Newtonian Fluid Mech. **142**, 4 (2007).

[13] E. Rabinowicz, *Friction and Wear of Materials*, (Wiley, New York, 1965).

[14] J. R. Rice and A. L. Ruina, J. Appl. Mech. **50**, 343 (1983).

[15] P. Zamankhan and M-H Bordbar, J. Appl. Mech. (T-ASME), **73**, 648 (2006).

[16] G. T. Mase and G. E. Mase, *Continuum Mechanics for Engineers* (CRC, Boca Raton, FL, 1999).

[17] H. Tennekes and J. L. Lumley, *A First Course in Turbulence* (MIT Press, Cambridge, MA, 1991).

[18] G. R. Liu, *Mesh Free Methods* (CRC, Boca Raton, FL, 2003); P. Zamankhan, Commun. Nonlin. Sci. Numer. Simul. **15**, 1538 (2010).

[19] D. Avnir, O. Biham, D. Lidar, and O. Malcai, Science **279**, 39 (1998).

[20] T. A. Witten and L. M. Sander, Phys. Rev. Lett. **47**, 1400 (1981).

[21] D. Tang and A. G. Marangoni, Chem. Phys. Lett. **433**, 248 (2006).

[22] M. P. Allen and D. J. Tildesley, *Computer Simulation of Liquids* (Oxford University Press, Oxford, 1987); L. E. Silbert, D. Ertas, G. S. Grest, T. C. Halsey, D. Levine, and S. J. Plimpton, Phys. Rev. E **64**, 051302 (2001).

[23] I. Goldhirsch and T. P. C. van Noije, Phys. Rev. E **61**, 3241 (2000).

[24] P. Zamankhan, Phys. Rev. E **52**, 4877 (1995).

[25] R. E. Rosensweig, *Ferrohydrodynamics* (Dover, New York, 1985).

[26] P. G. Saffman, J. Fluid Mech. **22**, 385 (1965); R. Mei, Int. J. Multiphase Flow **18**, 145 (1992).

[27] B. Oesterle and T. Bui Dinh, Exp. Fluids **25**, 16 (1998).

[28] M. R. Maxey and J. J. Riley, Phys. Fluids **26**, 883 (1983).

[29] *Chemical Engineers' Handbook*, 7th ed., edited by D. W. Green and R. H. Perry (McGraw Hill, New York, 2006); A. Jafari, P. Zamankhan, S. M. Mousavi, and K. Pietarnen, Chem. Eng. J. **144**, 476 (2008).

[30] I. Kececioglu and Y. Jiang,Trans. ASME: J. Fluids Eng. **116**, 164 (1994).

[31] S. Sundaresan, AIChE J. **46**, 1102 (2000).

[32] E. Loth and A. J. Dorgan, Br. Environ. Fluid Mech. **9**, 187 (2009).

[33] M. Lance and J. Bataille, J. Fluid Mech. **222**, 95 (1991).

[34] W. von Kroll, Forsh. Gebiete Ingeneiurw. **20**, 2 (1954).

[35] S. Ergun, Chem. Eng. Prog. **48**, 89 (1952).

[36] C. Y. Wen and Y. H. Yu, Chem. Eng. Prog. Symp. Ser. **62**, 100 (1966).

[37] P. S. Addison, *The Illustrated Wavelet Transform Handbook* (IOP, Bristol, UK, 2002).

[38] S. Sundaresan, Annu. Rev. Fluid Mech. **35**, 63 (2003).

[39] P. Zamankhan, P. Malinen, and H. Lepomäki, AIChE J. **43**, 1684 (1997).

[40] Y. J. Huang, C. K. Chan, and P. Zamankhan, Phys. Rev. E **82**, 031307 (2010)